Chemosphere 245 (2020) 125659

Contents lists available at ScienceDirect

Chemosphere

journal homepage: www.elsevier.com/locate/chemosphere

Polyaniline modified MIL-100(Fe) for enhanced photocatalytic Cr(VI) reduction and tetracycline degradation under white light

Dan-Dan Chen, Xiao-Hong Yi, Chen Zhao, Huifen Fu, Peng Wang, Chong-Chen Wang*

Beijing Key Laboratory of Functional Materials for Building Structure and Environment Remediation, Beijing University of Civil Engineering and Architecture, Beijing, 100044, China

HIGHLIGHTS

- The Z-scheme MIL-100(Fe)/PANI (MPx%) photocatalysts were facilely synthesized.
- MP9% exhibited superior photocatalytic activity toward Cr(VI) and tetracycline.
- MIL-100(Fe)/PANI composites demonstrated good reusability and stability.
- Z-scheme mechanism was proposed to clarify the improved photocatalytic activity.

GRAPHICAL ABSTRACT

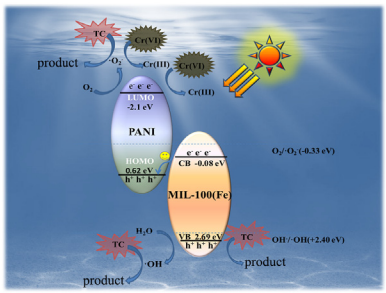

ARTICLE INFO

Article history:
Received 11 October 2019
Received in revised form
5 December 2019
Accepted 12 December 2019
Available online 14 December 2019

Handling Editor: Jun Huang

Keywords:
MIL-100(Fe)
Polyaniline
Z-Scheme photocatalyst
Cr(VI) reduction
Tetracycline degradation

ABSTRACT

The Z-scheme MIL-100(Fe)/PANI composite photocatalysts were facilely prepared from MIL-100(Fe) and polyaniline (PANI) by ball-milling, and were characterized by powder X-ray diffraction (PXRD), Fourier transform infrared spectroscopy (FTIR), thermogravimetric analysis (TGA), transmission electron microscopy (TEM), UV–visible diffuse-reflectance spectrometry (UV–vis DRS), X-ray photoelectron spectroscopy (XPS) and photoluminescence emission spectrometry (PL). The photocatalytic activities of MIL-100(Fe)/PANI composites were investigated via tetracycline degradation and hexavalent chromium reduction in aqueous solution under the irradiation of white light. The results revealed that the MIL-100(Fe)/PANI composite photocatalysts exhibited outstanding photocatalytic activities toward Cr(VI) reduction and tetracycline decomposition. The effects of pH and coexisting ions on the photocatalytic Cr(VI) reduction were investigated. As well, the primary active species were identified via electron spin resonance (ESR) determination. A possible Z-scheme photocatalyst mechanism was proposed and verified. Finally, MIL-100(Fe)/PANI composites demonstrated good reusability and stability in water solution, implying potentially practical applications for real wastewater treatment.

1. Introduction

Hexavalent chromium Cr(VI) is a typical pollutant in surface water and groundwater with high toxicity, high stability, high mobility and difficult to be degraded (Zhang et al., 2015b; Wang et al., 2016a), which became an important research topic in the treatment of wastewater and was included in the list of key pollutants by the U.S. Environmental Protection Agency (Zhang et al., 2015b; Jing et al., 2019). Conventional methods like adsorption, chemical precipitation, biological treatment, membrane filtration

* Corresponding author.
E-mail addresses: wangchongchen@bucea.edu.cn, chongchenwang@126.com (C.-C. Wang).

https://doi.org/10.1016/j.chemosphere.2019.125659
0045-6535/

were generally used to remove Cr(VI) from wastewater (Hu et al., 2005; Divrikli et al., 2007; Barrera, 2012; Wei et al., 2013; Gao et al., 2019; Thao et al., 2019), which were limited due to the disadvantages like mass sludge production, high chemical consumption, high processing cost, and poor sustainable development. Considering the conversion of solar energy, photocatalytic reduction is an effective and clean technology for reducing highly toxic Cr(VI) to lowly toxic Cr(III) (Liu et al., 2017a; Du et al., 2019a; Luo et al., 2019; Zhong et al., 2019; Li et al., 2020). Additionally, the wide use of antibiotics like tetracycline (TC) also exerted serious impact on the water environment (Wammer et al., 2011; Zou et al., 2019), which also imposed threats to human health due to the excessive accumulation of antibiotics in the human body, and they can induce kidney disease along with mutagenesis/teratogenic effects (Wang et al., 2018). Therefore, it is necessary to find an effective treatment to eliminate the emerging organic pollutants like antibiotics. The co-existence of antibiotics and heavy metal ions is a common phenomenon in sewage. Therefore, the simultaneous removal of antibiotics and toxic heavy metal ion was essential for sewage treatment.

Recently, metal-organic framework (MOFs) has attracted increasing attentions due to the wide applications including but not limited to gas storage/separation, molecular sensing and catalysis (Furukawa et al., 2013; Jeremias et al., 2013; Shen et al., 2013a,b; Yang et al., 2014; Yi et al., 2018; Feng et al., 2019). Especially, some MOFs were widely used as photocatalysts to achieve H_2 evolution (Wang et al., 2012), CO_2 reduction (Fu et al., 2012; Sun et al., 2013), Cr(VI) reduction (Liang et al., 2015c; Wang et al., 2016a, 2017a; Du et al., 2019a; Li et al., 2019; Zhao et al., 2019) and organic pollutants degradation (Wang et al., 2014, 2018). Generally, most Fe-containing MOFs displayed good photocatalytic performances under visible light irradiation due to the extensive Fe—O (iron-oxo) clusters (Han et al., 2018; Wang et al., 2019b), such as MIL-100, MIL-53, MIL-101, MIL-88A, MIL-88B (Du et al., 2011; Chen et al., 2014; Shi et al., 2015; Araya et al., 2017; Wang et al., 2017a). However, there are still some disadvantages like low conductivity, poor stability, and fast electron-hole recombination to limit their potential as efficient photocatalyst. To overcome the above-stated disadvantages of MOFs as photocatalysts, some semiconductors like titanium dioxide (TiO_2) (He et al., 2019; Wang et al., 2019a), graphitic carbon nitride (g-C_3N_4) (Du et al., 2019b; Wang et al., 2019b; Yi et al., 2019), silver phosphate (Ag_3PO_4) (Zhou et al., 2019) and even conductive polymers like polyaniline (PANI), polypyrrole (PPy) were adopted to modify the MOFs to increase the conductivity and promote the carrier separation, considering their non-toxic, low cost, significant optical and electrical properties (Chen et al., 2017; Liu et al., 2017; Han et al., 2018; Du et al., 2019).

Polyaniline (PANI) is one of the most promising conducting polymers with π-π conjugated structures, which arises increasing attention because of its low cost of monomer, facile synthesis, high conductivity, polar functional groups, and excellent environmental stability (Chen et al., 2014; Khan et al., 2018). As well, under visible light irradiation, PANI is not only an electron donor, but also an excellent hole acceptor (Lin et al., 2012). Some photocatalysts were modified by PANI to construct composites with enhanced photocatalytic performances, like PANI@TiO_2 (Liao et al., 2011; Lin et al., 2012), PANI@g-C_3N_4 (Ge et al., 2012), PANI@$MgIn_2S_4$ (Jing et al., 2019), PANI@ZnO (Zhang et al., 2009; Bao et al., 2019), and PANI@SnS_2 (Chen et al., 2017; Zhang et al., 2018). It can be found that a synergistic enhancement effect is accomplished from the combination between PANI and semiconductor photocatalyst, in which PANI can significantly improve the separation efficiency of photogenerated electron-hole pairs and then promote the photocatalytic activity (Chen et al., 2014). To the best of our current knowledge, up to now, only one case concerning PANI modified MOF composite was reported, in which PANI/FeUiO-66 nanohybrids with enhanced catalytic activity were utilized to accomplish the oxidation of aromatic alcohol under visible light (Xu et al., 2017). A facile strategy was introduced to fabricate stable MIL-100(Fe)/PANI composites with improved electrical conductivity and efficient charge carrier separation, which displayed superior photocatalytic activities toward Cr(VI) reduction and tetracycline degradation under the irradiation of white light. It was worthy to noting that the enhanced photocatalytic performances can be assigned to the formation of Z-scheme heterojunction. Finally, the corresponding Z-scheme mechanism of the photocatalytic reaction was verified via different techniques.

2. Experimental

2.1. Materials and instruments

All reagents were purchased from J&K and used directly without further purification, except that PANI (electric conductivity: 2 s/cm; molecular weight: 50,000−60,000) was bought from Taizhou Yongjia Trade Co. Ltd. XRD and FTIR of PANI are similar to literature reported (Liu et al., 2017b), The various characterization methods were listed in supporting information.

2.2. Preparation of MIL-100(Fe)/PANI composites

MIL-100(Fe) was prepared according to the previous literature reported by Horcajada and coworkers (Horcajada et al., 2007). In a typical synthesis, 0.139 g Fe^0, 0.344 g 1,3,5-benzenetricarboxylic acid (H_3BTC), 0.1 mL HF, 0.1 mL HNO_3, and 10.0 mL H_2O were mixed and sealed in a 25.0 mL Teflon-lined autoclave and heated at 150 °C for 3 d. The yellow MIL-100(Fe) powder was obtained by filtration and washed with deionized water. A further treatment in hot water (80 °C) for 3 h was carried out to remove unreacted H_3BTC. Then, the obtained powder was washed with deionized water, centrifuged at 5000 rpm for 5 min, and finally dried under vacuum at 60 °C for 12 h.

MIL-100(Fe)/PANI composites are synthesized by a simple ball-milling method at 30 Hz for 20 min. Schematic diagram of the synthesis process is shown in Scheme 1. In a typical experiment, 100 mg MIL-100(Fe) was mixed in a stainless-steel ball mill tanks with 3 mg, 5 mg, 7 mg, 9 mg PANI, respectively, under identical conditions. The obtained dark green MIL-100(Fe)/PANI composite powder were labeled as MP3%, MP5%, MP7% and MP9%, respectively.

2.3. Electrochemical measurements

Electrochemical measurements were analyzed using the Metrohm Autolab PGSTAT204 electrochemical station with 0.2 mol/L Na_2SO_4 aqueous solution (pH = 7.0) as the electrolyte in a typical three-electrode mode. The working electrode was prepared following the procedure: 5.0 mg MIL-100(Fe) or MIL-100(Fe)/PANI composite powders were mixed with 300.0 μL ethanol/Nafion (v/v = 19/1) under sonication for 30 min. 30.0 μL as-prepared slurry was casted onto the surface of a FTO substrate (1.0 cm × 1.0 cm) as thin film via drop casting method and then dried in air for 30 min. Finally, the working electrode was successfully fabricated after this process was repeated for several times to obtain smooth and uniform coating. A Pt electrode and a saturated Ag/AgCl electrode were used for the counter electrode and reference electrode respectively. Electrochemical impedance spectroscopy (EIS) measurements were carried out in dark, with frequencies of 500, 1000 and 1500 Hz, respectively. The transient photocurrent responses was measured

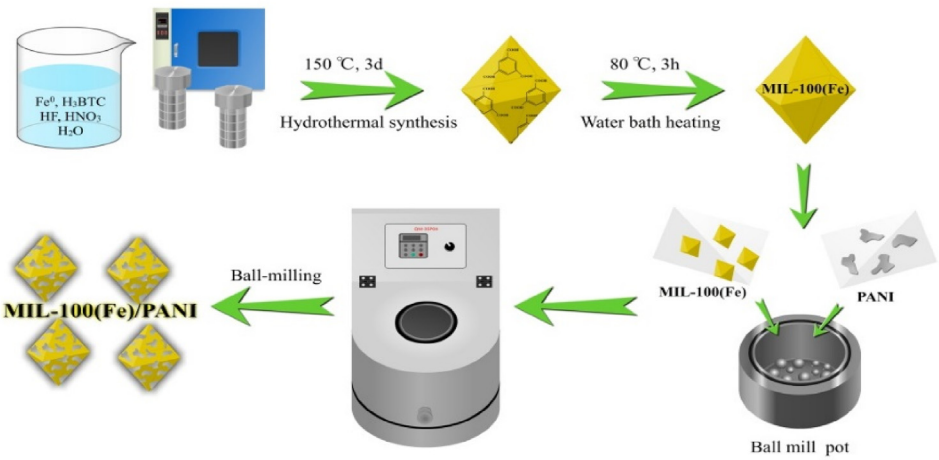

Scheme 1. The preparation procedure illustration of MIL-100(Fe)/PANI composites.

upon the illumination of 300 W Xenon lamp (Beijing Aulight Co., Ltd) as the white light source.

2.4. Photocatalytic activity evaluation

The 300 W xenon lamp (Beijing Aulight Co. Ltd.) was used as light source to conduct photocatalytic experiments, and the spectrum of the light source is shown in Fig. S1. The photocatalytic Cr(VI) reduction and TC degradation were carried out at 298 K in a photochemical reactor (Fig. S2) under the irradiation of white light. 50.0 mg photocatalyst was added to 200.0 mL Cr(VI) aqueous solution with the initial concentration of Cr(VI) being 10 mg L^{-1}. After stirring for 60 min to achieve adsorption-desorption equilibrium between photocatalysts and Cr(VI), the suspension was exposed to white light under magnetic stirring. 2.5 mL solution was taken out every 15 min and filtered using a 0.45 μm filter for further analysis. The Cr(VI) concentration was measured using diphenylcarbazide (DPC) method on AutoAnalyzer 3 Flow Injection Analyzer (instrument photograph was in Fig. S3). The desired pH of the solution was adjusted using H_2SO_4 (0.2 mol/L) or NaOH solution (0.2 mol/L), respectively.

The photocatalytic TC degradation activities over MIL-100(Fe)/PANI composites were also investigated. In experiments, 50.0 mg photocatalyst powder was dispersed in 200.0 mL TC aqueous solution (10 mg L^{-1}). After stirring in the dark for 60 min to accomplish adsorption - desorption equilibrium, the suspension was irradiated by the white light with xenon lamp. 2.5 mL suspension was drawn at every 15 min intervals using a 0.22 μm filter to remove the photocatalyst particles for analysis. An Acquity UPLC H-Class (Waters) system was used to detect the residual concentration of TC after the photocatalytic degradation. The analytes were separated on a C18 (1.7 μm, 2.1 mm × 50 mm) column in a UPLC system equipped with a TUV detector. UPLC determination method of tetracycline was listed as the following: aqueous phosphoric acid (0.1%) and methyl alcohol were used as mobile phases A and B, respectively. The gradient was programmed as: 0–2 min, 90–70% A; 2–4 min, 70–90% A; 4–4.5 min, 90–90% A. The column temperature was maintained at 30 °C, and the detector was set at the wavelength of 268 nm.

3. Results and discussion

3.1. Characterization

The PXRD patterns of MIL-100(Fe), PANI and series MIL-100(Fe)/PANI composites were illustrated in Fig. 1a. The PXRD patterns of MIL-100(Fe) were consistent with both the simulated ones from its single crystal data and those reported in the literature (Horcajada et al., 2007; Liang et al., 2015b), indicating that the prepared MIL-100(Fe) was pure and well crystallized. The characteristic peaks at $2\theta = 6.2°$, 10.2° and 11.0° were assigned to MIL-100(Fe) in the MIL-100(Fe)/PANI samples. No obvious diffraction peaks of PANI were observed in the PXRD patterns of MIL-100(Fe)/PANI composites, which was probably attributed to the relatively low content of PANI in the composites (Shen et al., 2013a), and amorphous phase of PANI (Li et al., 2008; Xiong et al., 2012). It implied that the PANI modification exerted no noticeable effect on the crystal structure of MIL-100(Fe).

The FTIR spectra of PANI, MIL-100(Fe) and MIL-100(Fe)/PANI composites were also performed to confirm the successful construction of MIL-100(Fe)/PANI composites. As illustrated in Fig. 1b, the broad peak at 3400 cm^{-1} is associated to the O–H vibration in MIL-100(Fe) (Xu et al., 2017), and the peaks at ca. 1708 cm^{-1}, 1574 cm^{-1} and 1113 cm^{-1} were corresponded to the C=O stretching vibrations of the carboxylate (Zhang et al., 2015a), C=C stretching vibration of the benzenoid rings (Hu et al., 2010) and C–O stretching vibration in H_3BTC (Xu et al., 2017), respectively. The peak at ca. 1477 cm^{-1} was attributed to C=C stretching of the quinonoid and benzenoid rings of PANI (Liao et al., 2011). Also, and the band at 798 cm^{-1} was related with C–H and C=C in benzenoid. The band at 1303 cm^{-1} was related to the C–N in the secondary aromatic amines (Chen et al., 2019). As well, the absorption peak of 1148 cm^{-1} was associated with stretching vibrations of $B–NH^{+}=Q$ in the quinonoid unit of PANI (Chen et al., 2019). The characteristic absorption peaks of MIL-100(Fe)/PANI composite and MIL-100(Fe) are similar, except for the low PANI content in the MIL-100(Fe)/PANI composites.

The UV–vis DRS are widely used to clarify the optical properties of the photocatalysts (Xu et al., 2017). As shown in Fig. 1c and d, the light absorption edge of pure MIL-100(Fe) was 600 nm, corresponding to a band gap (E_g) of 2.77 eV, consistent with literature reports (Ahmad et al., 2019). The MIL-100(Fe)/PANI composites exhibited stronger visible light response than the pristine MIL-100(Fe). As well, the band edge of MIL-100(Fe)/PANI composites

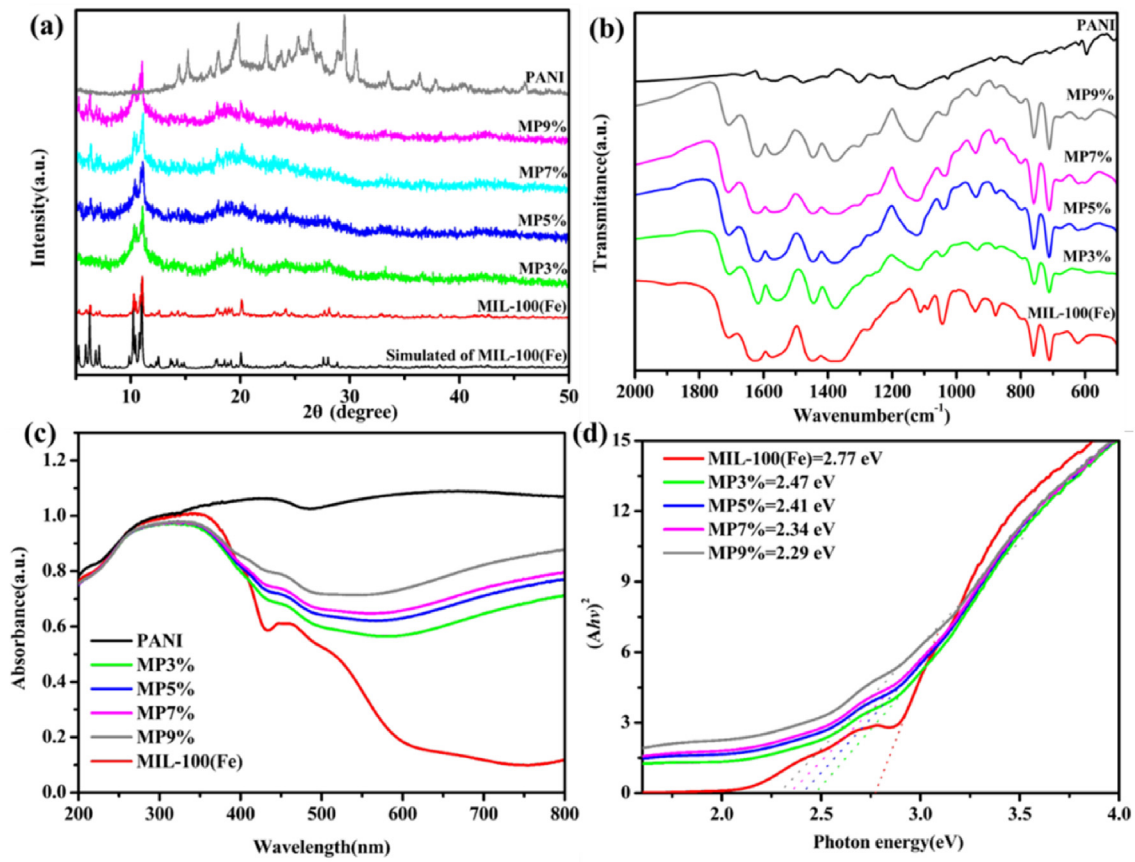

Fig. 1. (a)XRD patterns of MIL-100(Fe), simulated of MIL-100(Fe), PANI, and MIL-100(Fe)/PANI photocatalysts, (b)FTIR spectra of MIL-100(Fe), PANI, and MIL-100(Fe)/PANI photocatalysts, (c) and (d) UV–Vis diffuses reflectance spectra and $(Ah\nu)^2$ versus photon energy ($h\nu$) plots of the samples, respectively.

displayed a slight red shift from 2.77 eV for individual MIL-100(Fe) to 2.47, 2.41, 2.34, 2.29 eV for MP3%, MP5%, MP7%, MP9%, respectively. The relatively narrow band gap energy of MIL-100(Fe)/PANI composites may be due to the strong interactions of the hybrid structures formed between MIL-100(Fe) and PANI, which allow for more efficient utilization of the white light.

The morphologies and microstructures of the synthesized samples were observed by both SEM and TEM. The SEM and TEM images of the pure MIL-100(Fe) crystals were depicted in Fig. 2a, which exhibited regular polyhedrons or octahedrons morphology with smooth surface (Yoon et al., 2010; Fu et al., 2013). The SEM and TEM image of PANI (Fig. 2b) demonstrated the fibrous morphological structures along with agglomerated structures or a large number of interconnected tubules, which is consistent with previous literatures (Parveen et al., 2016; Ramohlola et al., 2018). From the SEM and TEM images of MP9% (Fig. 2c), it was observed that the PANI was uniformly coated on the surface of MIL-100(Fe) particles, which was further confirmed by HRTEM (Fig. 2d). However, the fringe spacings of MIL-100(Fe) and PANI in the composite couldn't be observed from HRTEM image due to their low crystalline quality (Chen et al., 2014; Zheng and Jiao, 2017; Wang et al., 2019b). The elemental (N, Fe and O) mapping obtained from SEM verified that PANI containing N elemental is evenly distributed on the surface of MIL-100(Fe) (Fig. 2e).

Further analysis of the XPS data provided detailed information about valence state and the chemical composition of MP9%. XPS survey scan indicated the presence of O, N, C and Fe elements in the composite sample, as shown in Fig. 3a. The C 1*s* spectrum of MP9% can be divided into three peaks centered at 284.8, 286.2, and 288.7 eV (Fig. 3b), in which may be assigned to C=C and C–N–C (Wang et al., 2019b) in PANI along with the O–C=O in H_3BTC ligand in MIL-100(Fe) (Wang et al., 2015; Xu et al., 2017; Zhang et al., 2018), respectively. The N 1*s* spectrum of MP9% can be split into two distinct curves (Fig. 3c): the peak at 399.9 eV was assigned to –NH– bond and the other peak at 401.9 eV was attributed to protonated amine units (-NH_2^+-) from PANI (Parveen et al., 2016; Wang et al., 2017b). The O 1*s* peak at 531.7 eV is attributed to the oxygen atoms in the carboxylate groups of the H_3BTC linkers of MIL-100(Fe) (Yang et al., 2016), as shown in Fig. 3d. Furthermore, the Fe 2*p* spectrum could be deconvoluted into four peaks in Fig. 3e. The binding energies of 711.9 and 726.3 eV are characteristic peak of Fe^{3+} in MIL-100(Fe) (Liang et al., 2015b), and the peak at 725.2 eV is assigned to the Fe $2p_{1/2}$ (Han et al., 2018). The satellite peak of Fe $2p_{3/2}$ at 716.3 eV is ascribed to the surface iron specie (Guo et al., 2010).

3.2. Photocatalytic performance

3.2.1. Photocatalytic activity for Cr(VI) reduction

The photocatalytic activities of the prepared composites towards Cr(VI) reduction were evaluated under white light illumination. As shown in Fig. 4a, the series of MIL-100/PANI composites demonstrated better photocatalytic activities towards Cr(VI) reduction than pristine MIL-100(Fe) or the mixture of MIL-100(Fe) and PANI under identical conditions. The MP9% composite photocatalyst exhibited better activity than the mixture of MIL-100(Fe) and PANI material (the content of two components is similar to MP9% without ball-milling), due to fabrication of the

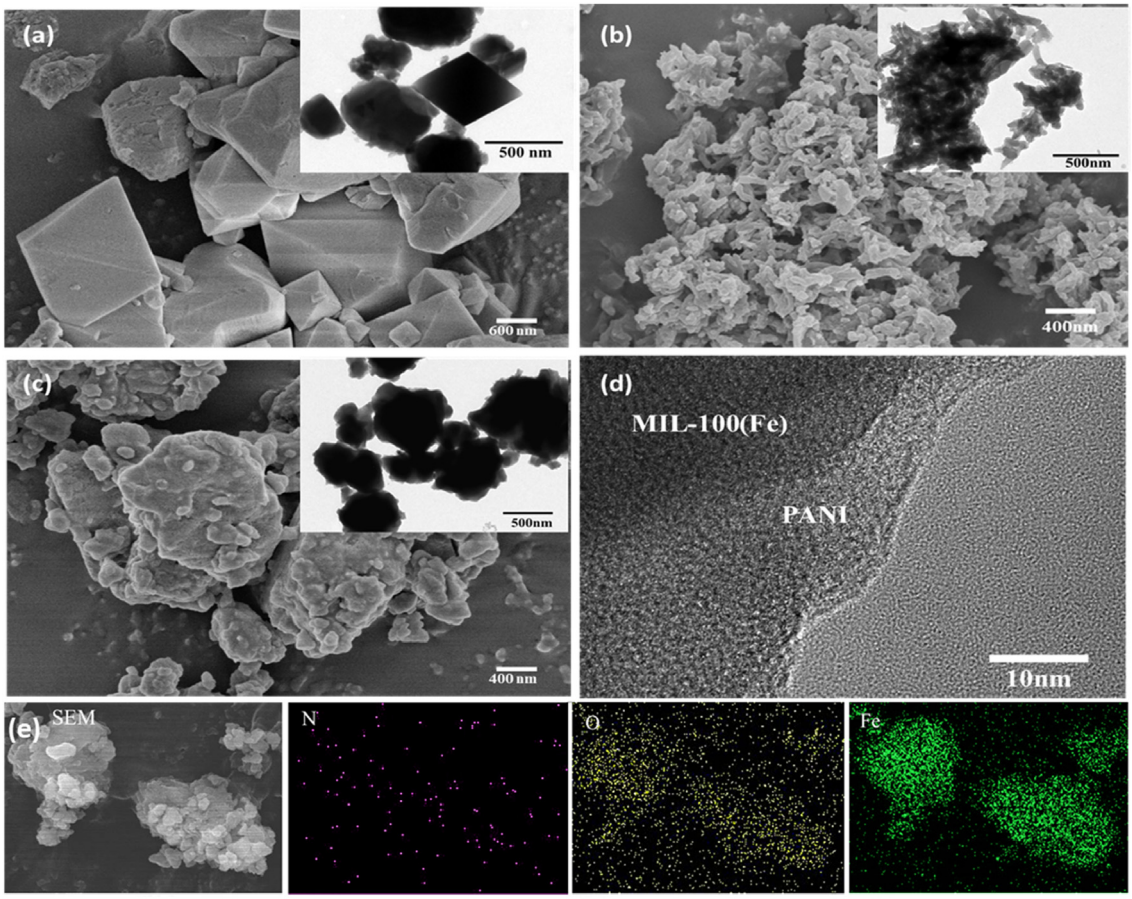

Fig. 2. The SEM images and the corresponding TEM images (inset) of (a) pure MIL-100(Fe), (b) PANI, (c) MP9%. (d) HRTEM image of MP9%, and (e) the elemental mapping of MP9%.

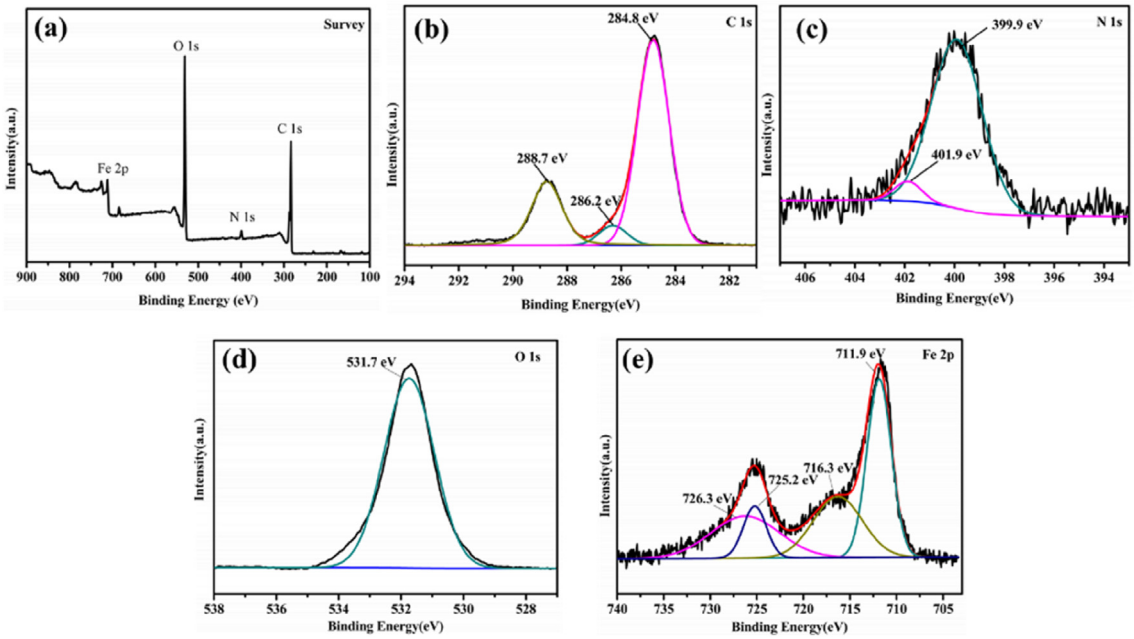

Fig. 3. XPS spectra of the MP9% composite: (a) survey scan; (b) C 1s; (c) N 1s; (d) O 1s; (e) Fe 2p.

heterojunctions between MIL-100(Fe) and PANI in MP9% (Jia et al., 2017). The MP9% composite demonstrated the best photocatalytic activity, evidenced by its Cr(VI) reduction efficiency of 100% within 90 min. Therefore, MP9% was selected as the photocatalyst

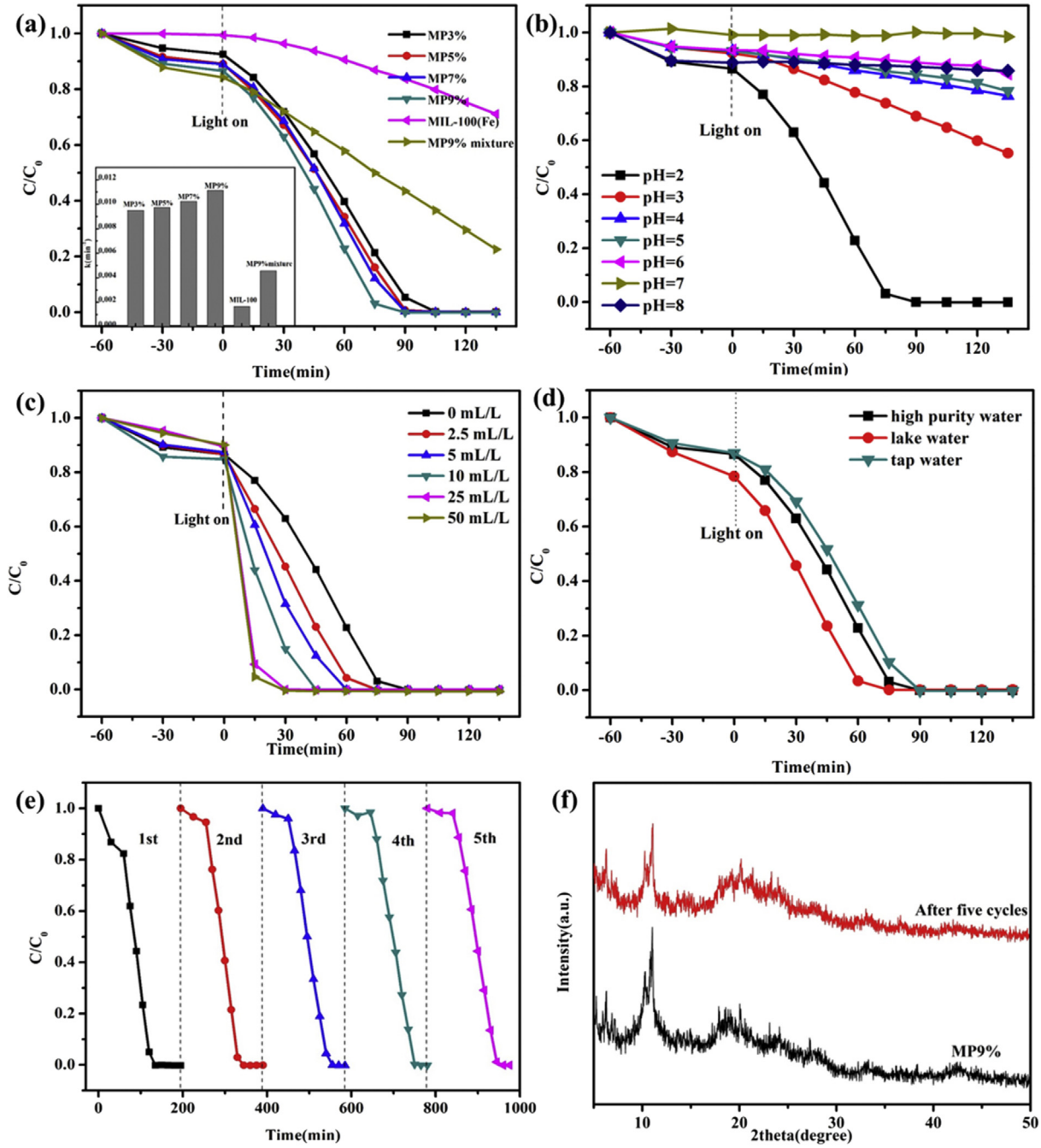

Fig. 4. (a) Photocatalytic Cr(VI) reduction performance of various photocatalysts and the reaction constants (inset); (b) Photocatalytic Cr(VI) reduction performance of MP9% at different pH values; (c) The influences of different ethanol concentrations toward photocatalytic Cr(VI) reduction activities of MP9%; (d) The influence of foreign ions in tap water and lake water on Cr(VI) reduction under white light; (e) Cyclic photocatalytic Cr(VI) reduction experiments of MP9%; (f) PXRD patterns of MP9% before and after five runs' cycle for photocatalytic Cr(VI) reduction.

candidate to further explore the effect of operating parameters on Cr(VI) reduction. To highlight the advantages of our as-prepared MIL-100(Fe)/PANI composite photocatalyst, some counterpart photocatalysts were selected to make a comparison (Table S1), in which the MP9% composite exhibited superior photocatalytic activity toward Cr(VI) reduction under the similar reaction conditions.

3.2.2. *Influence of initial pH value*

As widely accepted, the pH value of solution is an important factor to influence the photocatalytic Cr(VI) reduction (Liang et al., 2015b). The effect of pH on the Cr(VI) photoreduction over MP9% was investigated in the pH range from 2.0 to 8.0. As illustrated in Fig. 4b, with the increase of pH, the Cr(VI) reduction efficiency decreased rapidly (100%, 45%, 24%, 22%, 16%, 2% and 15% at pH = 2, 3, 4, 5, 6, 7 and 8, respectively) (Table S2). Under acidic conditions like pH being 2.0, the photocatalytic Cr(VI) reduction reaction follows Eq. (2), in which the abundant H^+ further facilitates the transformation from Cr(VI) to Cr(III) (Wang et al., 2016a). In alkaline environment, the main form of hexavalent chromium is CrO_4^{2-}, and

the reaction in the solution follows Eq. (3). In addition, when pH > 6, the formed $Cr(OH)_3$ precipitate will mask the active sites of MP9%, leading to the declined efficiency of photocatalytic Cr(VI) reduction (Ku and Jung, 2001; Liang et al., 2015a).

$$MPx\,\% + h\nu \rightarrow MPx\,\%\,(h^+ + e^-) \quad (1)$$

$$Cr_2O_7^{2-} + 14H^+ + 6e^- \rightarrow 2Cr^{3+} + 7H_2O \quad (2)$$

$$CrO_4^{2-} + 4H_2O + 3e^- \rightarrow Cr(OH)_3 + 5OH^- \quad (3)$$

3.2.3. Influence of holes scavengers

The consumption of holes (h^+) will accelerate photo-induced electron-hole charge separation and result in superior Cr(VI) reduction efficiency. Therefore, ethanol with different concentrations was introduced to capture the photo-generated holes. The results revealed that the efficiency of photocatalytic Cr(VI) reduction increased with the ethanol concentration (2.5, 5, 10, 25 and 50 mL/L) (Fig. 4c). It was considered that the added ethanol can consume the holes produced over the MP9% photocatalyst upon light irradiation to improve the separation of photo-induced electrons and holes (Eq. (4)) (Wang et al., 2019b).

$$CH_3CH_2OH + h^+ \rightarrow CO_2 + H_2O \quad (4)$$

3.2.4. Influence of foreign ions

In real wastewater, there are some co-exiting species like inorganic salts and even organics, which might affect the efficiency of photocatalytic Cr(VI) reduction (Wang et al., 2019b). In order to evaluate the practical application potential of MIL-100(Fe)/PANI composites, the simulated wastewater samples containing Cr(VI) prepared respectively with real tap water and lake water in Daxing campus of BUCEA were photocatalytically treated under white light irradiation. The water quality parameters of lake water and tap water were presented in the Table S3. As shown in Fig. 4d, the co-existing inorganic foreign ions exerted minor influence on the photocatalytic efficiency of Cr(VI) reduction up to 90 min. However, the photocatalytic reaction rate before 90 min followed the order of simulated wastewater prepared with lake water > pure water > tap water. As it was well known that inorganic ions like sodium ion, calcium ion in tap water (without organic matters) can decline the photocatalytic reaction, while co-existing inorganic ions and organic matters in lake water would balance the enhancement from organic matters and restriction from inorganic ions (Du et al., 2019a; Wang et al., 2019b).

3.2.5. Reusability and stability of MP9% toward Cr(VI) reduction under acidic conditions

The reusability of the photocatalyst is also very important for practical application. In our study, the photocatalytic cycling tests for Cr(VI) reduction were performed to investigate the reusability of MP9%. As demonstrated in Fig. 4e, the photocatalytic activity of MP9% toward Cr(VI) reduction was slightly reduced after 5 cycles, in which the Cr(VI) reduction efficiency could still reach 95% within 120 min. In this study, the leaching Fe ions in the aqueous solution after the 5th cyclic experiments were determined to be 5 ± 0.5 mg L^{-1}. As shown in Fig. 4f, the PXRD determination confirmed that the XRD patterns of MP9% after 5 runs matched perfectly with those of the as-prepared sample. As well, no noticeable changes were observed in the XPS spectra of MP9% composite before and after photocatalytic Cr(VI) reduction cycle experiments (Fig. S6). It was concluded that MP9% can be recycled and was stable during the photocatalytic reaction process.

3.3. Photocatalytic degradation of tetracycline

To further evaluate the photocatalytic oxidation behavior of MP9%, tetracycline (TC) was selected as organic pollutant model to perform degradation experiments under white light irradiation. As depicted in Fig. 5a, ca. 14% TC was degraded in the absence of MP9% up to 120 min under white light. Under the identical irradiations, 8%, 38%, 52% and 84% TC decompositions were accomplished with PANI, MIL-100(Fe), MIL-100(Fe)/PANI-9% mixture and MP9% as photocatalysts within 120 min (Table S4). In the absence of light irradiation, MP9% could achieve 38% elimination of TC via adsorption, which facilitated the final TC removal via photocatalytic degradation (Panneri et al., 2017).

3.4. Photocatalytic treatment toward simulated wastewater containing Cr(VI) and TC

The simulated wastewater containing both Cr(VI) and TC was adopted to test the photocatalytic performance of MP9% under pH = 2.0. As shown in Fig. 5b, the results revealed that the Cr(VI) reduction and TC decomposition were faster and more efficient in two-component system than that of the wastewater samples containing individual Cr(VI) or TC. In the two-component system, the Cr(VI) reduction and TC degradation efficiencies were 100% and 96% with 120 min, respectively. The Organic pollutant TC was used as the photogenerated holes scavenger and being oxidized, which promote the generation of photogenerated electrons and improve the reduction of Cr(VI) (Liang et al., 2015a).

3.5. Photocatalytic mechanism

Transient photocurrent responses were used to investigate the photoelectric responses of the photoelectrodes. As shown in Fig. 6a, under the identical conditions, MP9% produced much higher instantaneous photocurrent than MIL-100(Fe), due to that the hybridization effect in the MIL-100(Fe)/PANI composites can effectively promote light-induced charge transfer. The highly enhanced photocurrent response of MIL-100(Fe)/PANI could be attributed to both the superior charge mobility derived from the π-conjugation in the structure of PANI and the formation of a stable heterojunction between PANI and MIL-100(Fe) (Wang et al., 2017b). The electrochemical impedance spectra (EIS) of MIL-100(Fe) and MP9% were illustrated in Fig. 6b, in which the Nyquist arc radius of MP9% composite was smaller than that of MIL-100(Fe) under white light irradiation, implying that MP9% composite has a faster interfacial charge transfer and more efficient separation of photo-generated charge carriers than pure MIL-100(Fe) (Wang et al., 2017b). The PL spectra of MIL-100(Fe) and MP9% at an excitation wavelength of 345 nm were demonstrated in Fig. 6c. The PL intensity of MP9% at the 450 nm peak was weaker than that of pure MIL-100(Fe), implying that the recombination rate of photogenerated electrons and holes decreased in case of MP9%.

To explore the photocatalytic reaction mechanism, the ESR spin-trap experiment with DMPO technique was carried out to detect the main reactive species including $\bullet O_2^-$ and •OH involved in the photocatalytic process. As shown in Fig. 6e, no signal of $\bullet O_2^-$ can be observed in the dark, while under the white light irradiation for 5 or 10 min, the signals of DMPO-$\bullet O_2^-$ could be observed significantly. As well, the signals of •OH could be detected under the white light irradiation (Fig. 6f), and with the increase of irradiation time, the signal intensity of •OH increased obviously. It was concluded that

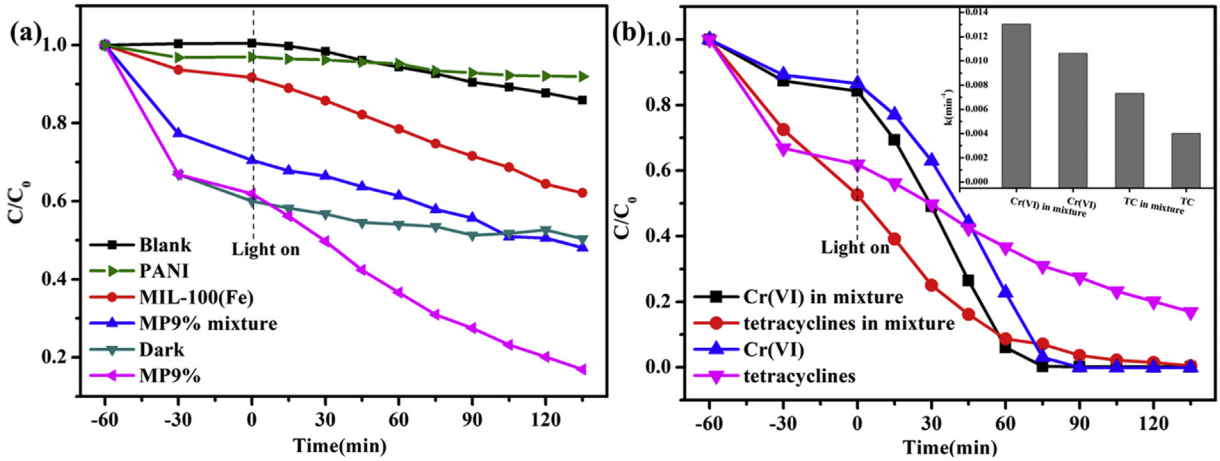

Fig. 5. (a) The variation of tetracycline concentration over various photocatalysts, (b) photocatalytic Cr(VI) reduction and TC degradation efficiencies in their single systems and in their matrix with MP9% as photocatalysts and the reaction constants (inset) under white light irradiation.

both •OH and $•O_2^-$ were formed during the photocatalytic process, which could degrade TC quickly (Yang et al., 2016; Wang et al., 2018, Wang et al., 2019b; Lu et al., 2019). Meanwhile, The potential to produce $•O_2^-$ (the LUMO of PANI) is more negative than the Cr(VI)/Cr(III) potential (+1.0 eV, pH = 2). It is theoretically permissible for the generated $•O_2^-$ to facilitate the transformation of Cr(VI) into Cr(III), as shown in Eq. (5). Besides, the N_2 gas was pumped to investigate the role of $•O_2^-$ in the photocatalytic system. The experimental results (Fig. S5) displayed obviously decreasing degradation efficiency during N_2 purging. The removal efficiency of Cr(VI) decreased from 100% under room condition) to 60% with N_2 purging with 90 min, indicating the significant role of $•O_2^-$ in the photocatalytic Cr(VI) reduction process. In addition, superoxide radicals ($•O_2^-$) mediated indirect reduction might govern the photoreduction of Cr(VI), according to previous literatures (Testa et al., 2001; Dong and Zhang, 2013; Hu et al., 2014, 2019; Wang et al., 2016b).

$$•O_2^- + Cr(VI) \rightarrow Cr(V) + O_2 \quad (5)$$

Zhu et al. reported that the MIL-100(Fe) is a p-type semiconductor (Ke et al., 2015; Zheng and Jiao, 2017), Therefore, the flat-band potentials of MIL-100(Fe) determined from Mott–Schottky plots are *ca.* −0.28 eV versus the Ag/AgCl electrode (equivalent to −0.08 eV vs. NHE) (Fig. 6d). The conduction bands (CB) (−0.08 eV) of MIL-100(Fe) is more negative than the Cr(VI)/Cr(III) potential (+1.0 eV, pH = 2 (Wang et al., 2004)). It is thermodynamically permissible for the transformation of photogenerated electrons to the Cr(VI) to produce Cr(III) (Liang et al., 2015a). The band gap value of MIL-100(Fe) estimated by UV–vis DRS is 2.77 eV. The valence band (VB) potential was calculated to be 2.69 eV vs. NHE. Besides, according to the literature, the LUMO and the HOMO potentials of PANI are −2.1 and 0.62 eV, respectively (Jing et al., 2019).

It is well known that both PANI and MIL-100(Fe) can be excited to generate electrons (e^-) and holes (h^+) under white light irradiation. Considering that the LUMO potential of PANI is more negative than CB of MIL-100(Fe), the photo-generated electrons of PANI can be easily migrated to the CB of MIL-100(Fe). Concurrently, the excited holes produced by MIL-100(Fe) are readily transferred into the HOMO of PANI. However, the HOMO (+0.62 eV) of PANI is more negative than the oxidation potential of OH^-/•OH (+2.40 eV). Meanwhile, the reduction potential of $O_2/•O_2^-$ (−0.33 eV) is more negative than that of CB potential (−0.08 eV) of MIL-100(Fe) (Li et al., 2018), indicating that the photoexcited electrons and holes cannot theoretically oxidize H_2O into •OH and combine O_2 to generate $•O_2^-$ (Zhu et al., 2017). But this mechanism could not match up with the highly photocatalytic performance of MIL-100(Fe)/PANI photocatalyst and ESR spin-trap test result, as shown in Fig. 7a. Therefore, the traditional photoinduced carrier transferring and separation mode is not suitable for this possible mechanism. As proposed in Fig. 7b, the energy gap (2.06 eV) between the LUMO orbital of PANI and the CB of MIL-100 (Fe) is larger than the energy gap (0.7 eV) between the CB of MIL-100 (Fe) to the HOMO of PANI. Therefore, the photogenerated electrons of MIL-100 (Fe) are more easily combined with the photoexcited holes on the HOMO orbit of the PANI (Li et al., 2018). At the same time, since the LUMO of PANI is more negative than the reduction potential of $O_2/•O_2^-$, and the VB (2.69 eV) of MIL-100 (Fe) is more positive than the oxidation potential of OH^-/•OH, the electrons generated over the LUMO of PANI are easy to reduce O_2 to $•O_2^-$ (Zhang et al., 2014; Zhu et al., 2017). The H_2O molecules were oxidized by the holes to form •OH over the VB of MIL-100(Fe). This Z-scheme mechanism of the charge transfer system is fully consistent with the results of the ESR spin-trap test. It was well known that the formation of Z-scheme type heterostructure is beneficial to improve photocatalytic activity (Xu et al., 2018). In our work, it could be concluded that the Cr(VI) was reduced into Cr(III) by both the electrons from LUMO of PANI, and the $•O_2^-$ formed between electrons and O_2 (Wang et al., 2016b; Zhang et al., 2018; Hu et al., 2019), and the tetracycline was decomposed not only directly by the holes accumulated on the VB of MIL-100(Fe), but also the secondarily formed reactive oxidative species like $•O_2^-$ and •OH (Yang et al., 2016; Wang et al., 2018; Du et al., 2019b; Lu et al., 2019).

PANI is an excellent material for transporting holes (h^+) and electrons (e^-) because of the specific π-conjugated structure (Xiong et al., 2012), inducing the separation of electrons and holes is accelerated, and formed a stable Z-scheme type heterostructure at the composite interface of MIL-100(Fe) and PANI, which contributes to significant activity of MIL-100(Fe)/PANI photocatalyst for the photocatalytic Cr(VI) reduction and tetracycline degradation. Therefore, charge transfer can effectively inhibit the recombination of the photo-generated electron-hole pairs, thus improving the photocatalytic activity of MIL-100(Fe)/PANI photocatalyst. The Z-scheme heterojunction formed in MIL-100 (Fe)/PANI composites made them quite different from the previously reported PANI/FeUiO-66 (Xu et al., 2017).

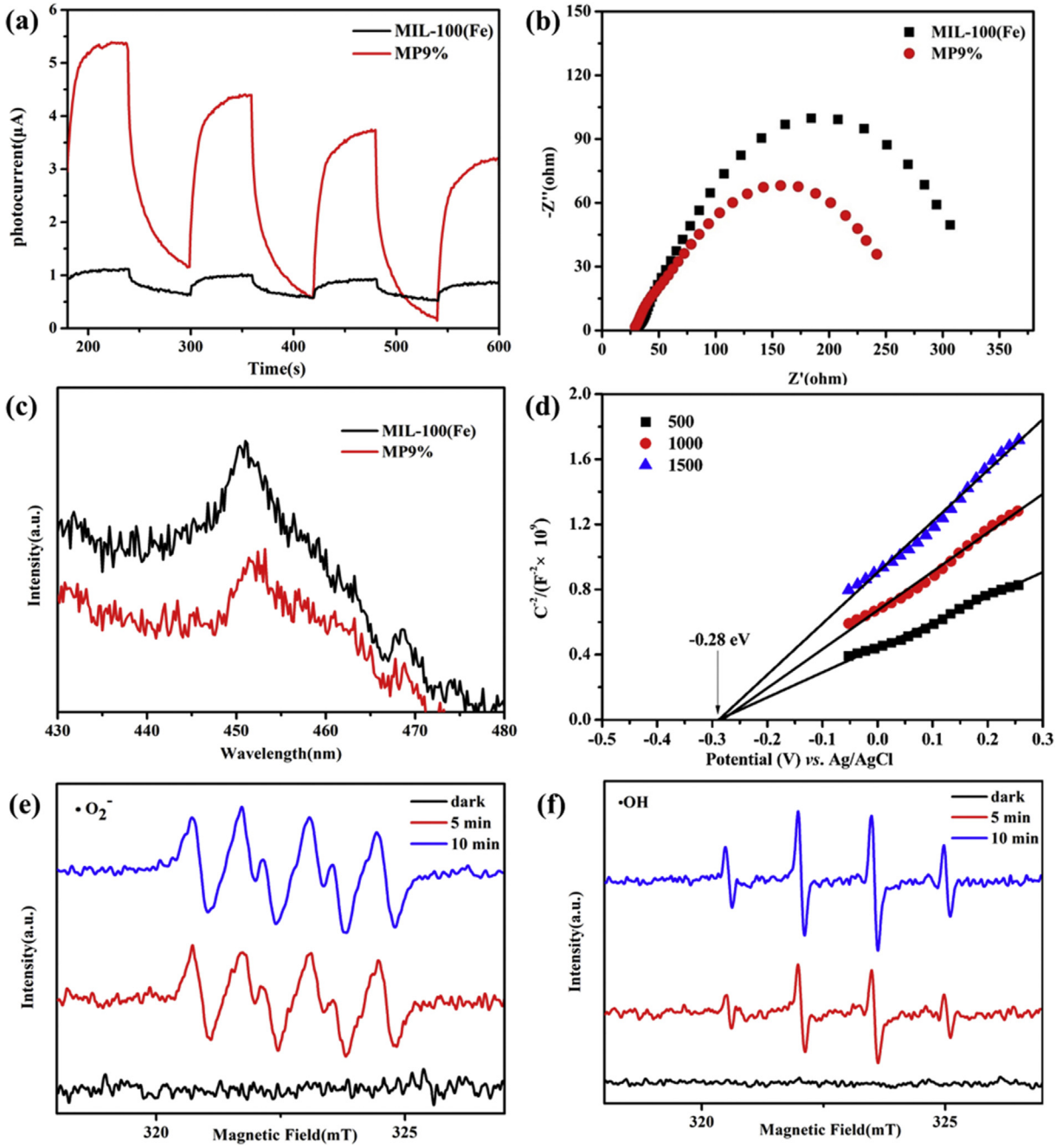

Fig. 6. (a) Transient photocurrent responses of MIL-100(Fe) and MP9%; (b) EIS plots of the samples under irradiation of white light; (c) Photoluminescence spectra of MIL-100(Fe) and MP9%; (d) Mott-Schottky plots of MIL-100(Fe) in 0.2 mol/L aqueous Na_2SO_4 solution (pH 7.0); ESR spectra of (e)·O_2^- and (f)·OH free radicals trapped by DMPO.

4. Conclusions

Series Z-scheme photocatalyst MIL-100(Fe)/PANI materials were facilely prepared by a ball-milling method. The obtained MP9% composite displayed superior photocatalytic activities toward Cr(VI) reduction (100%) and TC degradation (84%) under white light, which were 3.3 and 2.2 times higher than that of the pristine MIL-100(Fe). Electrochemical and ESR test results displayed that the enhanced photocatalytic performance was contributed to the Z-scheme heterojunction structure between MIL-100(Fe) and PANI, which promoted efficient transfer of photo-induced carrier charges. As well, the effect of pH, foreign ions on photocatalytic Cr(VI) reduction was explored. In addition, MP9% can achieve simultaneous elimination of Cr(VI) and TC due to the synergistic effect of electrons and holes. The cycle experiment of photocatalytic Cr(VI) reduction also demonstrated that MP9% was a stable and long term photocatalyst, which could be recycled and re-used for many times. It was anticipated that our work will provide new possibilities for PANI composites to form Z-scheme heterojunction and open a new door for broadening the application scope of MOFs as photocatalyst with the purpose to wastewater treatment.

Author contribution statement

Chen Dan-Dan: Data curation, Investigation, Visualization, Writing- Original draft preparation. **Yi Xiao-Hong:** Methodology,

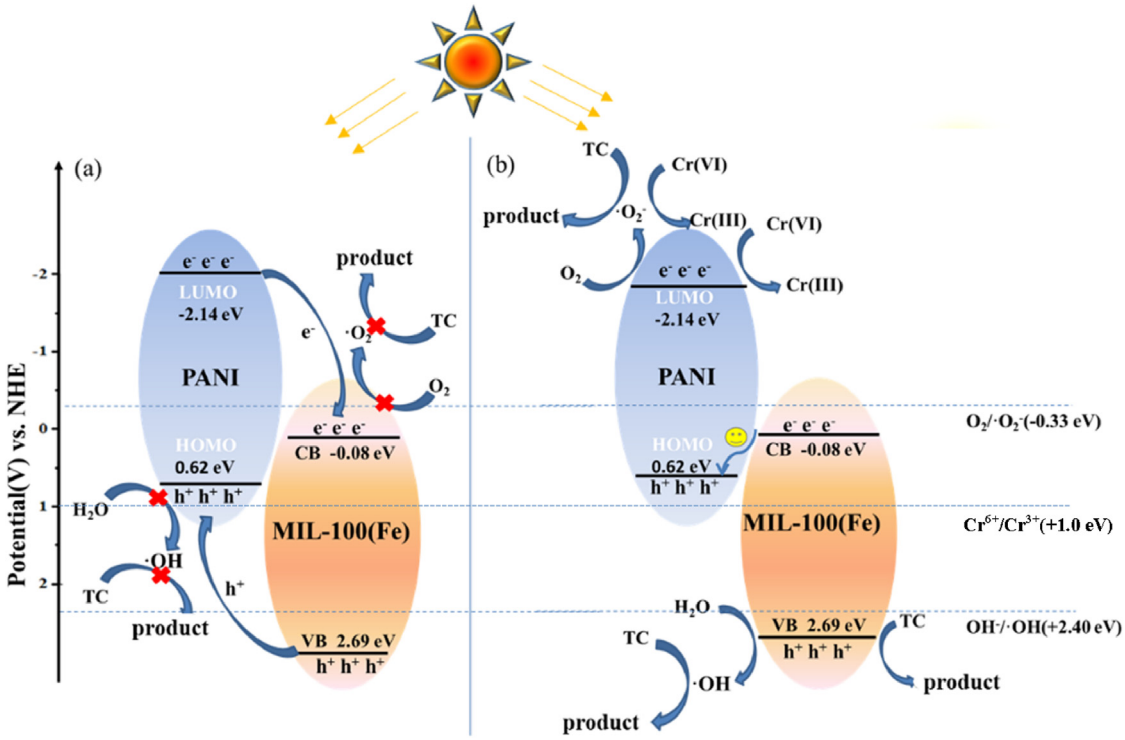

Fig. 7. Possible mechanism toward carrier migration and photocatalytic reaction of MIL-100(Fe)/PANI heterojunction photocatalyst: (a) conventional mode and (b) Z-scheme heterojunction system.

Software. **Zhao Chen:** Visualization, Software, Instrumental. **Fu Huifen:** Validation, Software. **Wang Peng:** Resources, Instrumental. **Wang Chong-Chen:** Conceptualization, Funding acquisition, Supervision, Project administration, Writing - review & editing.

Declaration of competing interest

On behalf of all authors, I declare that we do not have any commercial or associative interest that represents a conflict of interest in connection with the work entitled "Polyaniline modified MIL-100(Fe) for enhanced photocatalytic Cr(VI) reduction and tetracycline degradation under white light".

Acknowledgements

This work was supported by National Natural Science Foundation of China (51878023, 51578034), Beijing Municipal Natural Science Foundation, Great Wall Scholars Training Program Project of Beijing Municipality Universities (CIT&TCD20180323), Project of Construction of Innovation Teams and Teacher Career Development for Universities and Colleges Under Beijing Municipality (IDHT20170508), Beijing Talent Project (2019A22), and BUCEA Post Graduate Innovation Project (PG2019041).

Appendix A. Supplementary data

Supplementary data to this article can be found online at https://doi.org/10.1016/j.chemosphere.2019.125659.

References

Ahmad, M., Chen, S., Ye, F., Quan, X., Afzal, S., Yu, H., Zhao, X., 2019. Efficient photo-Fenton activity in mesoporous MIL-100(Fe) decorated with ZnO nanosphere for pollutants degradation. Appl. Catal. B Environ. 245, 428–438.
Araya, T., Jia, M., Yang, J., Zhao, P., Cai, K., Ma, W., Huang, Y., 2017. Resin modified MIL-53 (Fe) MOF for improvement of photocatalytic performance. Appl. Catal. B Environ. 203, 768–777.
Bao, C., Chen, M., Jin, X., Hu, D., Huang, Q., 2019. Efficient and stable photocatalytic reduction of aqueous hexavalent chromium ions by polyaniline surface-hybridized ZnO nanosheets. J. Mol. Liq. 279, 133–145.
Barrera, C.E., 2012. A review of chemical, electrochemical and biological methods for aqueous Cr(VI) reduction. J. Hazard Mater. 223–224, 1–12.
Chen, X., Zhang, M., Li, S., Li, L., Zhang, L., Wang, T., Yu, M., Mou, Z., Wang, C., 2017. Facile synthesis of polypyrrole@metal–organic framework core–shell nanocomposites for dual-mode imaging and synergistic chemo-photothermal therapy of cancer cells. J. Mater. Chem. B 5, 1772–1778.
Chen, Q., He, Q., Lv, M., Liu, X., Wang, J., Lv, J., 2014. The vital role of PANI for the enhanced photocatalytic activity of magnetically recyclable N–$K_2Ti_4O_9$/$MnFe_2O_4$/PANI composites. Appl. Surf. Sci. 311, 230–238.
Chen, Z., Wei, B., Yang, S., Li, Q., Liu, L., Yu, S., Wen, T., Hu, B., Chen, J., Wang, X., 2019. Synthesis of PANI/AlOOH composite for Cr(VI) adsorption and reduction from aqueous solutions. ChemistrySelect 4, 2352–2362.
Divrikli, U., Kartal, A.A., Soylak, M., Elci, L., 2007. Preconcentration of Pb(II), Cr(III), Cu(II), Ni(II) and Cd(II) ions in environmental samples by membrane filtration prior to their flame atomic absorption spectrometric determinations. J. Hazard Mater. 145, 459–464.
Dong, G., Zhang, L., 2013. Synthesis and enhanced Cr(VI) photoreduction property of formate anion containing graphitic carbon nitride. J. Phys. Chem. C 117, 4062–4068.
Du, X., Yi, X., Wang, P., Deng, J., Wang, C., 2019a. Enhanced photocatalytic Cr(VI) reduction and diclofenac sodium degradation under simulated sunlight irradiation over MIL-100(Fe)/g-C_3N_4 heterojunctions. Chin. J. Catal. 40, 70–79.
Du, X.-D., Yi, X.-H., Wang, P., Zheng, W., Deng, J., Wang, C.-C., 2019b. Robust photocatalytic reduction of Cr(VI) on UiO-66-NH_2(Zr/Hf) metal-organic framework membrane under sunlight irradiation. Chem. Eng. J. 356, 393–399.
Du, J.-J., Yuan, Y.-P., Sun, J.-X., Peng, F.-M., Jiang, X., Qiu, L.-G., Xie, A.-J., Shen, Y.-H., Zhu, J.-F., 2011. New photocatalysts based on MIL-53 metal–organic frameworks for the decolorization of methylene blue dye. J. Hazard Mater. 190, 945–951.
Feng, Y., Chen, Q., Cao, M., Ling, N., Yao, J., 2019. Defect-tailoring and titanium substitution in metal–organic framework UiO-66-NH_2 for the photocatalytic degradation of Cr(VI) to Cr(III). ACS Appl. Nano Mater. 2, 5973–5980.
Fu, Y.-Y., Yang, C.-X., Yan, X.-P., 2013. Metal-organic framework MIL-100(Fe) as the stationary phase for both normal-phase and reverse-phase high performance liquid chromatography. J. Chromatogr. A 1274, 137–144.
Fu, Y., Sun, D., Chen, Y., Huang, R., Ding, Z., Fu, X., Li, Z., 2012. An amine-functionalized titanium metal–organic framework photocatalyst with visible-light-induced activity for CO_2 reduction. Angew. Chem. Int. Ed. 51, 3364–3367.
Furukawa, H., Cordova, K.E., O'Keeffe, M., Yaghi, O.M., 2013. The chemistry and

applications of metal-organic frameworks. Science 341, 1230444.
Gao, J., Wu, Z., Chen, L., Xu, Z., Gao, W., Jia, G., Yao, Y., 2019. Synergistic effects of iron ion and PANI in biochar material for the efficient removal of Cr(VI). Mater. Lett. 240, 147–149.
Ge, L., Han, C., Liu, J., 2012. In situ synthesis and enhanced visible light photocatalytic activities of novel PANI–g-C_3N_4 composite photocatalysts. J. Mater. Chem. 22, 11843–11850.
Guo, L., Chen, F., Fan, X., Cai, W., Zhang, J., 2010. S-doped α-Fe_2O_3 as a highly active heterogeneous Fenton-like catalyst towards the degradation of acid orange 7 and phenol. Appl. Catal. B Environ. 96, 162–168.
Han, Y., Shi, H., Bai, C., Zhang, L., Wu, J., Meng, H., Xu, Y., Zhang, X., 2018. Ag_3PO_4-MIL-53(Fe) composites with visible-light-enhanced photocatalytic activities for rhodamine B degradation. ChemistrySelect 3, 8045–8050.
He, L., Dong, Y., Zheng, Y., Jia, Q., Shan, S., Zhang, Y., 2019. A novel magnetic MIL-101(Fe)/TiO_2 composite for photo degradation of tetracycline under solar light. J. Hazard Mater. 361, 85–94.
Horcajada, P., Surblé, S., Serre, C., Hong, D.-Y., Seo, Y.-K., Chang, J.-S., Grenèche, J.-M., Margiolaki, I., Férey, G., 2007. Synthesis and catalytic properties of MIL-100(Fe), an iron(III) carboxylate with large pores. Chem. Commun. 2820–2822.
Hu, J., Cai, H., Ren, H., Wei, Y., Xu, Z., Liu, H., Hu, Y., 2010. Mixed-matrix membrane hollow fibers of $Cu_3(BTC)_2$ MOF and polyimide for gas separation and adsorption. Ind. Eng. Chem. Res. 49, 12605–12612.
Hu, J., Chen, G., Lo, I.M.C., 2005. Removal and recovery of Cr(VI) from wastewater by maghemite nanoparticles. Water Res. 39, 4528–4536.
Hu, X., Ji, H., Chang, F., Luo, Y., 2014. Simultaneous photocatalytic Cr(VI) reduction and 2,4,6-TCP oxidation over g-C_3N_4 under visible light irradiation. Catal. Today 224, 34–40.
Hu, X., Wang, W., Xie, G., Wang, H., Tan, X., Jin, Q., Zhou, D., Zhao, Y., 2019. Ternary assembly of g-C_3N_4/graphene oxide sheets/$BiFeO_3$ heterojunction with enhanced photoreduction of Cr(VI) under visible-light irradiation. Chemosphere 216, 733–741.
Jeremias, F., Lozan, V., Henninger, S.K., Janiak, C., 2013. Programming MOFs for water sorption: amino-functionalized MIL-125 and UiO-66 for heat transformation and heat storage applications. Dalton Trans. 42, 15967–15973.
Jia, Y., Niu, X., An, S., Chen, W., Liu, W., 2017. Facile synthesis of Bi_2MoO_6 –MIL-100(Fe) metal–organic framework composites with enhanced photocatalytic performance. RSC Adv. 7, 2943–2952.
Jing, L., Xu, Y., Xie, M., Liu, J., Deng, J., Huang, L., Xu, H., Li, H., 2019. Three dimensional polyaniline/$MgIn_2S_4$ nanoflower photocatalysts accelerated interfacial charge transfer for the photoreduction of Cr(VI), photodegradation of organic pollution and photocatalytic H_2 production. Chem. Eng. J. 360, 1601–1612.
Ke, F., Wang, L., Zhu, J., 2015. Facile fabrication of CdS-metal-organic framework nanocomposites with enhanced visible-light photocatalytic activity for organic transformation. Nano Res. 8, 1834–1846.
Khan, N.A., Yoo, D.K., Jhung, S.H., 2018. Polyaniline-encapsulated metal–organic framework MIL-101: adsorbent with record-high adsorption capacity for the removal of both basic quinoline and neutral indole from liquid fuel. ACS Appl. Mater. Interfaces 10, 35639–35646.
Ku, Y., Jung, I.-L., 2001. Photocatalytic reduction of Cr(VI) in aqueous solutions by UV irradiation with the presence of titanium dioxide. Water Res. 35, 135–142.
Li, B., Lai, C., Zeng, G., Qin, L., Yi, H., Huang, D., Zhou, C., Liu, X., Cheng, M., Xu, P., Zhang, C., Huang, F., Liu, S., 2018. Facile hydrothermal synthesis of Z-scheme $Bi_2Fe_4O_9$/Bi_2WO_6 heterojunction photocatalyst with enhanced visible light photocatalytic activity. ACS Appl. Mater. Interfaces 10, 18824–18836.
Li, M., Qiu, J., Yang, L., Feng, Y., Yao, J., 2020. Fabrication of TiO_2 embedded $ZnIn_2S_4$ nanosheets for efficient Cr(VI) reduction. Mater. Res. Bull. 122, 110671.
Li, X., Wang, D., Cheng, G., Luo, Q., An, J., Wang, Y., 2008. Preparation of polyaniline-modified TiO_2 nanoparticles and their photocatalytic activity under visible light illumination. Appl. Catal. B Environ. 81, 267–273.
Li, Y.-X., Fu, H., Wang, P., Zhao, C., Liu, W., Wang, C.-C., 2019. Porous tube-like ZnS derived from rod-like ZIF-L for photocatalytic Cr(VI) reduction and organic pollutants degradation. Environ. Pollut. 113417.
Liang, R., Jing, F., Shen, L., Qin, N., Wu, L., 2015a. MIL-53(Fe) as a highly efficient bifunctional photocatalyst for the simultaneous reduction of Cr(VI) and oxidation of dyes. J. Hazard Mater. 287, 364–372.
Liang, R., Luo, S., Jing, F., Shen, L., Qin, N., Wu, L., 2015b. A simple strategy for fabrication of Pd@MIL-100(Fe) nanocomposite as a visible-light-driven photocatalyst for the treatment of pharmaceuticals and personal care products (PPCPs). Appl. Catal. B Environ. 176–177, 240–248.
Liang, R., Shen, L., Jing, F., Wu, W., Qin, N., Lin, R., Wu, L., 2015c. NH_2-mediated indium metal–organic framework as a novel visible-light-driven photocatalyst for reduction of the aqueous Cr(VI). Appl. Catal. B Environ. 162, 245–251.
Liao, G., Chen, S., Quan, X., Zhang, Y., Zhao, H., 2011. Remarkable improvement of visible light photocatalysis with PANI modified core–shell mesoporous TiO_2 microspheres. Appl. Catal. B Environ. 102, 126–131.
Lin, Y., Li, D., Hu, J., Xiao, G., Wang, J., Li, W., Fu, X., 2012. Highly efficient photocatalytic degradation of organic pollutants by PANI-modified TiO_2 composite. J. Phys. Chem. C 116, 5764–5772.
Liu, S., Chen, F., Li, S., Peng, X., Xiong, Y., 2017c. Enhanced photocatalytic conversion of greenhouse gas CO_2 into solar fuels over g-C_3N_4 nanotubes with decorated transparent ZIF-8 nanoclusters. Appl. Catal. B Environ. 211, 1–10.
Liu, L., Ding, L., Liu, Y., An, W., Lin, S., Liang, Y., Cui, W., 2017b. A stable Ag_3PO_4@PANI core@shell hybrid: enrichment photocatalytic degradation with π-π conjugation. Appl. Catal. B Environ. 201, 92–104.
Liu, F., Yu, J., Tu, G., Qu, L., Xiao, J., Liu, Y., Wang, L., Lei, J., Zhang, J., 2017a. Carbon nitride coupled Ti-SBA15 catalyst for visible-light-driven photocatalytic reduction of Cr (VI) and the synergistic oxidation of phenol. Appl. Catal. B Environ. 201, 1–11.
Lu, Z., Peng, J., Song, M., Liu, Y., Liu, X., Huo, P., Dong, H., Yuan, S., Ma, Z., Han, S., 2019. Improved recyclability and selectivity of environment-friendly MFA-based heterojunction imprinted photocatalyst for secondary pollution free tetracycline orientation degradation. Chem. Eng. J. 360, 1262–1276.
Luo, J., Zhang, S., Sun, M., Yang, L., Luo, S., Crittenden, J.C., 2019. A critical review on energy conversion and environmental remediation of photocatalysts with remodeling crystal lattice, surface, and interface. ACS Nano 13, 9811–9840.
Panneri, S., Thomas, M., Ganguly, P., Nair, B.N., Mohamed, A.P., Warrier, K.G.K., Hareesh, U.S., 2017. C_3N_4 anchored ZIF 8 composites: photo-regenerable, high capacity sorbents as adsorptive photocatalysts for the effective removal of tetracycline from water. Catal. Sci. Technol. 7, 2118–2128.
Parveen, N., Mahato, N., Ansari, M.O., Cho, M.H., 2016. Enhanced electrochemical behavior and hydrophobicity of crystalline polyaniline@graphene nanocomposite synthesized at elevated temperature. Compos. B Eng. 87, 281–290.
Ramohlola, K.E., Monana, G.R., Hato, M.J., Modibane, K.D., Molapo, K.M., Masikini, M., Mduli, S.B., Iwuoha, E.I., 2018. Polyaniline-metal organic framework nanocomposite as an efficient electrocatalyst for hydrogen evolution reaction. Compos. B Eng. 137, 129–139.
Shen, L., Liang, S., Wu, W., Liang, R., Wu, L., 2013a. Multifunctional NH_2-mediated zirconium metal–organic framework as an efficient visible-light-driven photocatalyst for selective oxidation of alcohols and reduction of aqueous Cr(vi). Dalton Trans. 42, 13649–13657.
Shen, L., Wu, W., Liang, R., Lin, R., Wu, L., 2013b. Highly dispersed palladium nanoparticles anchored on UiO-66(NH_2) metal-organic framework as a reusable and dual functional visible-light-driven photocatalyst. Nanoscale 5, 9374–9382.
Shi, L., Wang, T., Zhang, H., Chang, K., Meng, X., Liu, H., Ye, J., 2015. An amine-functionalized iron(III) metal-organic framework as efficient visible-light photocatalyst for Cr(VI) reduction. Adv. Sci. 2, 1500006.
Sun, D., Fu, Y., Liu, W., Ye, L., Wang, D., Yang, L., Fu, X., Li, Z., 2013. Studies on photocatalytic CO_2 reduction over NH_2-uio-66(Zr) and its derivatives: towards a better understanding of photocatalysis on metal–organic frameworks. Chem. Eur J. 19, 14279–14285.
Testa, J.J., Grela, M.A., Litter, M.I., 2001. Experimental evidence in favor of an initial one-electron-transfer process in the heterogeneous photocatalytic reduction of chromium(VI) over TiO_2. Langmuir 17, 3515–3517.
Thao, V.D., Giang, B.L., Thu, T.V., 2019. Free-standing polypyrrole/polyaniline composite film fabricated by interfacial polymerization at the vapor/liquid interface for enhanced hexavalent chromium adsorption. RSC Adv. 9, 5445–5452.
Wammer, K.H., Slattery, M.T., Stemig, A.M., Ditty, J.L., 2011. Tetracycline photolysis in natural waters: loss of antibacterial activity. Chemosphere 85, 1505–1510.
Wang, C.-C., Du, X.-D., Li, J., Guo, X.-X., Wang, P., Zhang, J., 2016a. Photocatalytic Cr(VI) reduction in metal-organic frameworks: a mini-review. Appl. Catal. B Environ. 193, 198–216.
Wang, C.-C., Li, J.-R., Lv, X.-L., Zhang, Y.-Q., Guo, G., 2014. Photocatalytic organic pollutants degradation in metal–organic frameworks. Energy Environ. Sci. 7, 2831–2867.
Wang, D., Jia, F., Wang, H., Chen, F., Fang, Y., Dong, W., Zeng, G., Li, X., Yang, Q., Yuan, X., 2018. Simultaneously efficient adsorption and photocatalytic degradation of tetracycline by Fe-based MOFs. J. Colloid Interface Sci. 519, 273–284.
Wang, C.-C., Wang, X., Liu, W., 2019a. The synthesis strategies and photocatalytic performances of TiO_2/MOFs composites: a state-of-the-art review. Chem. Eng. J. 123601.
Wang, C.-C., Yi, X.-H., Wang, P., 2019b. Powerful combination of MOFs and C_3N_4 for enhanced photocatalytic performance. Appl. Catal. B Environ. 247, 24–48.
Wang, F.-X., Yi, X.-H., Wang, C.-C., Deng, J.-G., 2017a. Photocatalytic Cr(VI) reduction and organic-pollutant degradation in a stable 2D coordination polymer. Chin. J. Catal. 38, 2141–2149.
Wang, H., Yuan, X., Wu, Y., Zeng, G., Chen, X., Leng, L., Li, H., 2015. Synthesis and applications of novel graphitic carbon nitride/metal-organic frameworks mesoporous photocatalyst for dyes removal. Appl. Catal. B Environ. 174–175, 445–454.
Wang, J.-L., Wang, C., Lin, W., 2012. Metal–organic frameworks for light harvesting and photocatalysis. ACS Catal. 2, 2630–2640.
Wang, X., Pehkonen, S.O., Ray, A.K., 2004. Removal of aqueous Cr(VI) by a combination of photocatalytic reduction and coprecipitation. Ind. Eng. Chem. Res. 43, 1665–1672.
Wang, J.-C., Ren, J., Yao, H.-C., Zhang, L., Wang, J.-S., Zang, S.-Q., Han, L.-F., Li, Z.-J., 2016b. Synergistic photocatalysis of Cr(VI) reduction and 4-Chlorophenol degradation over hydroxylated α-Fe_2O_3 under visible light irradiation. J. Hazard Mater. 311, 11–19.
Wang, Y., Wang, L., Huang, W., Zhang, T., Hu, X., Perman, J.A., Ma, S., 2017b. A metal–organic framework and conducting polymer based electrochemical sensor for high performance cadmium ion detection. J. Mater. Chem. 5, 8385–8393.
Wei, X., Kong, X., Wang, S., Xiang, H., Wang, J., Chen, J., 2013. Removal of heavy metals from electroplating wastewater by thin-film composite nanofiltration hollow-fiber membranes. Ind. Eng. Chem. Res. 52, 17583–17590.
Xiong, P., Chen, Q., He, M., Sun, X., Wang, X., 2012. Cobalt ferrite–polyaniline heteroarchitecture: a magnetically recyclable photocatalyst with highly enhanced performances. J. Mater. Chem. 22, 17485–17493.
Xu, Q., Zhang, L., Yu, J., Wageh, S., Al-Ghamdi, A.A., Jaroniec, M., 2018. Direct Z-scheme photocatalysts: principles, synthesis, and applications. Mater. Today 21,

1042–1063.
Xu, X., Liu, R., Cui, Y., Liang, X., Lei, C., Meng, S., Ma, Y., Lei, Z., Yang, Z., 2017. PANI/FeUiO-66 nanohybrids with enhanced visible-light promoted photocatalytic activity for the selectively aerobic oxidation of aromatic alcohols. Appl. Catal. B Environ. 210, 484–494.
Yang, Y., Wang, F., Yang, Q., Hu, Y., Yan, H., Chen, Y.-Z., Liu, H., Zhang, G., Lu, J., Jiang, H.-L., Xu, H., 2014. Hollow metal–organic framework nanospheres via emulsion-based interfacial synthesis and their application in size-selective catalysis. ACS Appl. Mater. Interfaces 6, 18163–18171.
Yang, Z., Xu, X., Liang, X., Lei, C., Wei, Y., He, P., Lv, B., Ma, H., Lei, Z., 2016. MIL-53(Fe)-graphene nanocomposites: efficient visible-light photocatalysts for the selective oxidation of alcohols. Appl. Catal. B Environ. 198, 112–123.
Yi, X.-H., Ma, S.-Q., Du, X.-D., Zhao, C., Fu, H., Wang, P., Wang, C.-C., 2019. The facile fabrication of 2D/3D Z-scheme g-C_3N_4/UiO-66 heterojunction with enhanced photocatalytic Cr(VI) reduction performance under white light. Chem. Eng. J. 375, 121944.
Yi, X.-H., Wang, F.-X., Du, X.-D., Fu, H., Wang, C.-C., 2018. Highly efficient photocatalytic Cr(VI) reduction and organic pollutants degradation of two new bifunctional 2D Cd/Co-based MOFs. Polyhedron 152, 216–224.
Yoon, J.W., Seo, Y.-K., Hwang, Y.K., Chang, J.-S., Leclerc, H., Wuttke, S., Bazin, P., Vimont, A., Daturi, M., Bloch, E., Llewellyn, P.L., Serre, C., Horcajada, P., Grenèche, J.-M., Rodrigues, A.E., Férey, G., 2010. Controlled reducibility of a metal–organic framework with coordinatively unsaturated sites for preferential gas sorption. Angew. Chem. Int. Ed. 49, 5949–5952.
Zhang, H., Zong, R., Zhu, Y., 2009. Photocorrosion inhibition and photoactivity enhancement for zinc oxide via hybridization with monolayer polyaniline. J. Phys. Chem. C 113, 4605–4611.
Zhang, J., Hu, Y., Jiang, X., Chen, S., Meng, S., Fu, X., 2014. Design of a direct Z-scheme photocatalyst: preparation and characterization of Bi_2O_3/g-C_3N_4 with high visible light activity. J. Hazard Mater. 280, 713–722.
Zhang, F., Jin, Y., Shi, J., Zhong, Y., Zhu, W., El-Shall, M.S., 2015a. Polyoxometalates confined in the mesoporous cages of metal–organic framework MIL-100(Fe): efficient heterogeneous catalysts for esterification and acetalization reactions. Chem. Eng. J. 269, 236–244.
Zhang, Y., Zhang, Q., Shi, Q., Cai, Z., Yang, Z., 2015b. Acid-treated g-C_3N_4 with improved photocatalytic performance in the reduction of aqueous Cr(VI) under visible-light. Separ. Purif. Technol. 142, 251–257.
Zhang, F., Zhang, Y., Zhang, G., Yang, Z., Dionysiou, D.D., Zhu, A., 2018. Exceptional synergistic enhancement of the photocatalytic activity of SnS_2 by coupling with polyaniline and N-doped reduced graphene oxide. Appl. Catal. B Environ. 236, 53–63.
Zhao, C., Wang, Z., Li, X., Yi, X., Chu, H., Chen, X., Wang, C.-C., 2019. Facile fabrication of BUC-21/$Bi_{24}O_{31}Br_{10}$ composites for enhanced photocatalytic Cr(VI) reduction under white light. Chem. Eng. J. 123431.
Zheng, J., Jiao, Z., 2017. Modified Bi_2WO_6 with metal-organic frameworks for enhanced photocatalytic activity under visible light. J. Colloid Interface Sci. 488, 234–239.
Zhong, J., Yi, X.-H., Wang, P., Wang, C.-C., 2019. A stable 1D mixed-valence CuI/CuII coordination polymer with photocatalytic reduction activity toward Cr(VI). J. Mol. Struct. 1183, 256–262.
Zhou, Y.-C., Xu, X.-Y., Wang, P., Fu, H., Zhao, C., Wang, C.-C., 2019. Facile fabrication and enhanced photocatalytic performance of visible light responsive UiO-66-NH_2/Ag_2CO_3 composite. Chin. J. Catal. 40 (2019), 1912–1923, 1912-1923.
Zhu, B., Xia, P., Li, Y., Ho, W., Yu, J., 2017. Fabrication and photocatalytic activity enhanced mechanism of direct Z-scheme g-C_3N_4/Ag_2WO_4 photocatalyst. Appl. Surf. Sci. 391, 175–183.
Zou, J.-P., Chen, Y., Liu, S.-S., Xing, Q.-J., Dong, W.-H., Luo, X.-B., Dai, W.-L., Xiao, X., Luo, J.-M., Crittenden, J., 2019. Electrochemical oxidation and advanced oxidation processes using a 3D hexagonal Co_3O_4 array anode for 4-nitrophenol decomposition coupled with simultaneous CO_2 conversion to liquid fuels via a flower-like CuO cathode. Water Res. 150, 330–339.